Microkinetic Model Fitted with a Genetic Algorithm to Experimental XPS Coverages at High Pressure-CO Hydrogenation on Rh(111)

(article starts on next page)

Article

Microkinetic Model Fitted with a Genetic Algorithm to Experimental XPS Coverages at High Pressure−CO Hydrogenation on Rh(111)

Published as part of The Journal of Physical Chemistry C virtual special issue "Jens K. Nørskov Festschrift".

Mikael Valter-Lithander, Minttu Kauppinen, David Degerman, Gabriel L. S. Rodrigues, Henrik Grönbeck, and Lars G. M. Pettersson*

Read Online

ACCESS | 📊 Metrics & More | 📖 Article Recommendations | SI Supporting Information

ABSTRACT: Comparisons to experiments are important when developing kinetic models based on density functional theory (DFT) calculations. The comparisons are, however, often challenging due to the assumed uncertainties in the energies from which the kinetic parameters are calculated. Here, we introduce a genetic algorithm to adjust the DFT-energies to better match experimental XPS data, using CO hydrogenation on Rh(111) as an example. The adjustments are made to adsorption energies, adsorbate−adsorbate interactions, XPS energies, and peak shapes. While these parameters improve the experimental agreement considerably, the required changes to the DFT energies are relatively large, which indicates the need for refined treatments of, for example, possible surface species and reaction steps, surface inhomogeneities, or higher levels of electronic structure calculations. We propose the genetic-algorithm based method as a general tool for assessment of computational models.
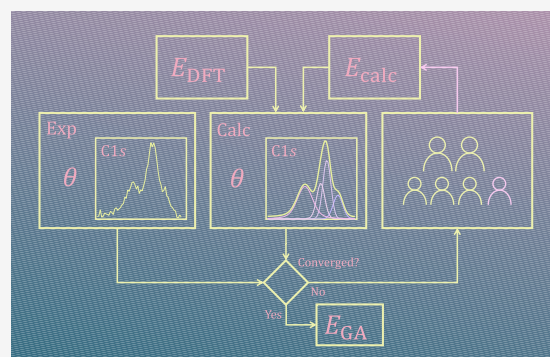
INTRODUCTION

Computational methods are an integrated part of heterogeneous catalysis research as they provide atomistic understanding of reaction mechanisms and can be used to guide the development of new catalytic materials.[1] In this respect, electronic structure calculations based on density functional theory (DFT) play a major role as a means to calculate local energy minima and reaction barriers, which form the basis for first-principles-based microkinetic modeling (MKM).[2,3] While DFT calculations have proven very useful to develop conceptual understanding and to study trends, there are intrinsic limitations in the accuracy. Chemical accuracy is typically out of reach, which may significantly affect computed rates and even the predicted reaction pathways. To target these issues and obtain estimates of the uncertainties in the predicted energetics, the Bayesian Error Estimate Functional (BEEF)[4] with van der Waals correction has been applied to provide error estimates for the parameters.[1,5,6] These have then been used to generate an ensemble of MKM:s using parameters spanning the uncertainties from which error estimates of the resulting rates can be derived.[5,7] The predicted rates or yields can subsequently be compared to experiment to verify the reliability of the constructed MKM and its kinetic parameters in terms of interaction energies, reaction barriers and pre-exponential factors.[8,9]

For each possible reaction path, the highest barriers often have rate control. Thus, it is generally sufficient to establish these with high precision, assuming that the other barriers are reasonably beyond the bounds set by the accuracy of the applied DFT scheme. A general approach to reach the required accuracy has recently been proposed for reactions on transition-metals by Araujo et al.,[10] on insulators and in physisorption on Pt(111) by Sauer and co-workers[11−13] through a combination of DFT-calculations with periodic boundary conditions and corrections from higher-accuracy methods on smaller cluster models. However, full consideration of even a simple reaction as hydrogenation of CO on Rh(111) involves more than 100 potential species and 2000 possible reaction paths,[14] making it infeasible to treat all steps at the same high-accuracy level. This complexity has been addressed by Nørskov and co-workers[14] by, as a first step, building a surrogate model based on machine-learned adsorption energies, linear-scaling relationships and a classifier for the rate-limiting step along each path to find the overall competing reaction pathways and their rate-limiting barriers to which higher-level methods can then be applied. In this way, the complete reaction network can be investigated.
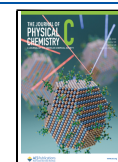
However, the approach relies on the assumption that the reaction conditions in terms of the character of the actual, active catalytic surface (facets, steps, defects, impurities, dynamics, etc.) are as postulated in the MKM. An alternative approach, which allows investigating assumptions in the MKM, has been proposed by Rangarajan et al.[15] where the residual in a fitness function against experimental rates and DFT energies is minimized. In a combined experimental and computational study this was applied to the decomposition of formic acid over various Pt/C catalysts.[16]

Here, we suggest and explore an additional route that has recently become possible through the availability of high-pressure X-ray photoelectron spectroscopy (XPS) data on intermediate species during the reaction. The spectra contain information about the *operando* resting state of the catalyst, in which species before the rate-limiting step are amassed to a higher degree than species after the rate-limiting step. Consequently, the coverages provide information that is intuitively linked to the actual mechanistic pathway of the reaction. Thus, instead of focusing on rates or yields, which depend sensitively on the computed DFT energies, we take an agnostic attitude toward their accuracy. This entails developing and applying a genetic algorithm (GA) to evolve the computed adsorption energies and barriers in the MKM to match the steady-state coverages on the catalytic surface during operating (temperature and pressure) conditions. Combining the results with the knowledge of uncertainties in computed DFT values, the comparison between experimental and theoretical coverages makes it possible to investigate modeling assumptions in the MKM as well as the accuracy of specific values that the GA changes beyond expected error bars. In addition, if such outliers persist, this information can be an indication that the MKM needs to be extended with additional side reactions and to question whether the catalyst under reaction conditions remains as assumed in the model.

XPS can be used to determine the *operando* surface coverage of a reaction. Traditionally, this has only been possible at low pressures, but with a recent setup from Amann and co-workers,[17] measurements can be performed at pressures around 1 bar, which is close or closer to realistic reaction conditions. This high-pressure setup has been applied to investigate, e.g., CO hydrogenation on Ni,[18] carbide formation in Fischer–Tropsch synthesis on Fe(110),[19] CO and CO_2 hydrogenation on stepped Rh(211),[20] the Haber-Bosch process,[21] and methanol synthesis over Zn/ZnO/Cu(211).[22] Here, we focus on measurements of coverages of oxygen- and carbon-containing species on Rh(111) during CO hydrogenation at 150 mbar and temperatures from 175 to 325 °C.[23] In the case of carbon spectra, the resolution is sufficient to distinguish several peaks, to which groups of surface species can be assigned based on their different experimental or computed C $1s$ XPS binding energies.

CO hydrogenation on Rh(111) is an important reaction that has been the topic of several DFT studies in combination with MKM.[5–7,14,24,25] Here, we use the now available XPS data to illustrate a systematic approach to assess theoretical models and DFT data, by building an MKM for CO hydrogenation and using a genetic algorithm (GA) to modify computed energies and barriers, such that coverages deduced from the XPS spectra are reproduced. Knowledge of the steady-state coverages during the reaction gives stronger constraints on the parameters of an MKM model than when only the overall (temperature- and pressure-dependent) rate is compared to experimental data.

Naturally, if the rate of the target reaction has been measured, the GA and MKM can be constrained even further. If the assumptions of the MKM are consistent with the actual experimental conditions and reaction network, and the parameters of the MKM (adsorption energies, reaction barriers and pre-exponential factors) are correctly obtained by the computational model, then the changes to these parameters generated by the GA are expected to be within the error bars of the applied computational model (typically DFT). In such a case, the accuracy can potentially be further improved by applying techniques to reduce the errors, such as suggested in refs.,[10–13] to determine the kinetic parameters for the critical steps, fix those at the calibrated values and allow the GA to readjust the remaining parameters in an iterative process.

If there are important reaction steps or interactions missing in the MKM or the wrong catalytic surface is assumed in the MKM, the GA will still attempt to fit the target, but now by changing the DFT computed parameters beyond expectation. When this happens, it is an indication to reevaluate the assumptions behind the constructed MKM after ensuring that the errant values have been computed correctly.

Key to a successful GA is the fitness function that specifies the target toward which the process evolves. Here, we mainly use the extracted temperature-dependent carbon and oxygen coverages and XPS spectra. The genes defining each individual in a step (generation) of the algorithm are at first simply the adsorption energies and reaction barriers that enter the MKM, with more variable parameters added if more complexity is needed. The first generation is populated by the required number of individuals with genes as random variations of the computed energetics. At each step, the MKM is solved for each individual and the result ranked according to the computed fitness. The more fit individuals, plus a random selection of individuals with lower fitness (to avoid inbreeding), are taken to generate the next generation by crossover, i.e. the first part of the new gene is taken up to a random point from the first randomly selected "parent" and the rest from the second randomly selected "parent". The "offspring" is thereafter subjected to random mutations and the thus generated new generation used as input to a new series of MKM models. To obtain results that are not completely unphysical, it is necessary to restrict the inputs, e.g., penalizing (by fitness contribution) or putting strict limits on the deviation from DFT energies. Importantly, the most fit individual(s) are transferred intact to the next generation as a guarantee that fitness can only improve. Like in evolution by natural selection, it is thus enough for an individual to not be among the least fit to be guaranteed to procreate and contribute its gene to the next generation.

METHODS

Energy Calculations for Minima and Transition States.

Density functional calculations for minima and transition states were performed using VASP5,[26–29] where the projector-augmented wave (PAW)[30] method was used to model the interactions between the valence electrons and the core. The Kohn–Sham orbitals were represented by a plane-wave basis set with 500 eV as cutoff energy and a Gaussian smearing of 0.05 eV applied to the Fermi level discontinuity. BEEF-vdW[4] was used as exchange-correlation functional.

The Rh(111) surface was modeled as four-layer p(3×3) slabs, separated by a vacuum of 20 Å and sampled with $(4,4,1)$ k-points in a Monkhorst–Pack grid. The gas phase species were computed in a $(20 \times 20 \times 20)$ Å cell using only the gamma point.

The quasi-Newton method was used for structure relaxations with a total residual force of 0.02 eV/Å as convergence criterion.

Transition states were calculated using the dimer method[31,32] or the climbing image nudged-elastic band method.[33] Vibrational modes were calculated by diagonalization of the Hessian matrix, where the derivatives of the forces were computed by means of the central difference approximation with a displacement of 0.05 Å. The energies for gas phase molecules, adsorbates and transition states are defined as formation energies from the stoichiometric amount of gas-phase CO, H_2 and H_2O and a clean Rh(111) surface.

XPS. Density functional calculations for XPS binding energies were performed with pairs of single-point calculations in VASP using 600 eV as cutoff on four-layer $p(4 \times 4)$ slabs with $(4,4,1)$ k-points. The number of calculated bands for the core-hole state was chosen to be $\frac{n_e}{2} + 150$, where n_e is the total number of electrons in the supercell, to allow proper relaxation of the valence; for ground state calculations, the default is enough. Other relevant parameters are the same as for the minima calculations above.

The XPS binding energy (BE) shifts were obtained by simulating a core-ionized state where the PAW potential included the explicit core-hole. The final BE was obtained using the expression

$$BE = E_{final} - E_{gs}$$

where E_{final} is the total electronic energy of the final (core-hole) state, and E_{gs} is the total electronic energy of the ground-state. Because of error cancelation, XPS shifts are more accurately computed than absolute XPS binding energies and are furthermore less sensitive to the choice of functional.[34] Thus, on-top CO was taken as computational reference and all computed XPS energies shifted such that the absolute value for CO coincided with the experimentally determined XPS value (C: 286.0 eV[35]).

A Shirley background[36] was subtracted between 282 and 288 eV prior to fitting, accounting for inelastic scattering of photoelectrons in the adsorbate layer and in the gas phase. XPS spectra were modeled assuming Gaussian broadening around the peak BE. A Lorentzian contribution to the peak shape was not considered here since the lifetime broadening of the compounds is relatively small in comparison to the Gaussian part of the peak shape. The broadening, i.e., the standard deviation σ of the normal distribution, is estimated from the experimental peak at 325 °C (in, e.g., Figure 2) to be 0.45 eV, which is used unless the broadening is allowed to vary. The experimental C 1s spectra and total coverages are taken from ref.[23] The reason that we do not use the O 1s spectra is that there was an overlap between the electron energy loss peak and the O spectra in the experiment. It also means that the accuracy of the total C coverages is higher than the total O coverages.
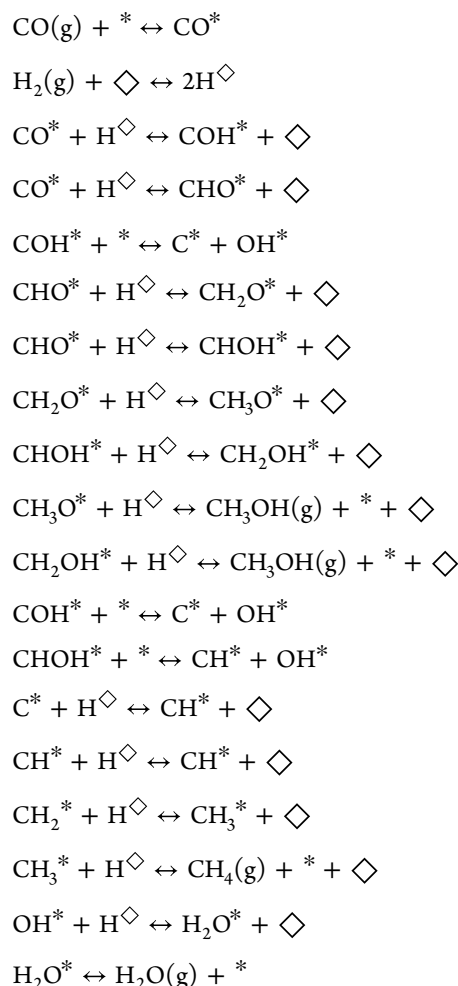
Microkinetic Model. A mean-field microkinetic model (MKM) without lateral adsorbate−adsorbate interactions results in a CO-poisoned surface, in contrast to experimental results. The reason for this is that the CO adsorption energy is coverage-dependent.[35] Thus, Yang et al.[5] introduced a DFT-based, piecewise linear adsorbate−adsorbate interaction for CO with itself and other intermediates. In the present work, we apply a simplified model with adsorbate−adsorbate interactions (AAI) included in a linear fashion, such that

$$E_S = E_{S,0} + \sum_A m_{S,A} \theta_A$$

where E_S is the differential adsorption energy of surface species S (adsorbate or transition state), $E_{S,0}$ the corresponding differential adsorption energy at zero coverage, θ_A the coverage of adsorbate A, and $m_{S,A}$ the linear parameter for the interaction between S and A. The parameter between two adsorbates is symmetric, i.e., $m_{A,B} = m_{B,A}$ where B is also an adsorbate. To further simplify the model, cross-interaction parameters between adsorbates were approximated as the average of the self-interaction parameters, i.e., $m_{A,B} = \frac{m_{A,A} + m_{B,B}}{2}$. This simple model can be compared to the piecewise linear model with smooth transitions used by Lausche et al.[37] and the second order expansion in coverage by Yang et al.[5]

A microkinetic model was constructed for the hydrogenation of CO to methane, water, and methanol. Note that higher carbon-containing (C_{2+}) species were not included. Similarly to Yang et al.[5] and Schumann et al.,[6] atomic hydrogen occupies up to 1 monolayer (ML) in a reservoir site ($\diamond$), while the rest of the adsorbates share a maximum of 1 ML on regular surface sites (*); hydrogen is, thus, assumed to not compete for sites while still affecting other species through AAI.

The following reactions were included in the model:

$$CO(g) + * \leftrightarrow CO^*$$

$$H_2(g) + \diamond \leftrightarrow 2H^\diamond$$

$$CO^* + H^\diamond \leftrightarrow COH^* + \diamond$$

$$CO^* + H^\diamond \leftrightarrow CHO^* + \diamond$$

$$COH^* + * \leftrightarrow C^* + OH^*$$

$$CHO^* + H^\diamond \leftrightarrow CH_2O^* + \diamond$$

$$CHO^* + H^\diamond \leftrightarrow CHOH^* + \diamond$$

$$CH_2O^* + H^\diamond \leftrightarrow CH_3O^* + \diamond$$

$$CHOH^* + H^\diamond \leftrightarrow CH_2OH^* + \diamond$$

$$CH_3O^* + H^\diamond \leftrightarrow CH_3OH(g) + * + \diamond$$

$$CH_2OH^* + H^\diamond \leftrightarrow CH_3OH(g) + * + \diamond$$

$$COH^* + * \leftrightarrow C^* + OH^*$$

$$CHOH^* + * \leftrightarrow CH^* + OH^*$$

$$C^* + H^\diamond \leftrightarrow CH^* + \diamond$$

$$CH^* + H^\diamond \leftrightarrow CH^* + \diamond$$

$$CH_2{}^* + H^\diamond \leftrightarrow CH_3{}^* + \diamond$$

$$CH_3{}^* + H^\diamond \leftrightarrow CH_4(g) + * + \diamond$$

$$OH^* + H^\diamond \leftrightarrow H_2O^* + \diamond$$

$$H_2O^* \leftrightarrow H_2O(g) + *$$

The resulting ordinary differential equations (ODEs) have the form:

$$\frac{d\theta_n}{dt} = \sum_i \nu_{n,i} r_i$$

where $\nu_{n,i}$ is the stoichiometric coefficient of species n in elementary reaction step i and r_i is the reaction rate of elementary reaction step i. The reaction rates are functions of rate constants k_i and species coverages θ_n. The forward and reverse rate constants k of the activated surface reactions were calculated according to the harmonic transition state theory (TST) with the Eyring-Polanyi equation:

$$k = \frac{k_B T}{h} e^{-G_a/k_B T}$$

where G_a is the activation free energy of the elementary step, T is temperature, and k_B and h are the Boltzmann and Planck's constants, respectively. The forward (reverse) activation free energy is the difference in the Gibbs free formation energy between the transition state and the reactant (product) species of a given elementary reaction. For the adsorption reactions the rate constants were calculated according to the Hertz-Knudsen equation:

$$k_{ads} = \frac{pA}{\sqrt{2\pi m T k_B}}$$

where p is the partial pressure of the gas phase species, A is the area of the adsorption site, and m is the mass of a single molecule of the gas. The Gibbs free energies of gas and surface species were calculated using the thermochemistry module found in the Atomic Simulation Environment (ASE) software package.[38] The gas species were treated in the ideal gas approximation, with translational, rotational and vibrational degrees of freedom considered independent. Surface intermediates and transition states were evaluated within the harmonic approximation which treats all degrees of freedom as harmonic vibrations. The mean-field microkinetic model, i.e. the set of ODEs, was solved with Python by numerical integration. Within this methodology, no assumptions on the rate controlling steps or most abundant surface species are made a priori. The numerical integration is carried out subject to initial conditions from time t = 0 until steady state, i.e., the surface coverages are no longer changing with time:

$$\frac{d\theta_n}{dt} = 0$$

The initial coverage of the surface species was set to zero or to the steady-state coverage of "adjacent" temperature, if available. The pressures of gas phase species were kept constant during the integration, the initial values being 100 mbar H_2 and 50 mbar CO as in the experiment. The numerical integration was performed using the solve_ivp function found in the Scipy package scipy.integrate.[39]

Genetic Algorithm. A genetic algorithm was used (see Figure 1) to modify the energies of the species, to which later AAI parameters and XPS peak and broadening parameters are added. The fitness function that should be minimized had four components:

1. Agreement between the output coverages from the MKM and the experimental XPS signal. The spectrum deviation averaged over data points and temperatures is denoted $\overline{S}$.

2. Agreement between output total coverage and total experimental coverages. The deviation between total
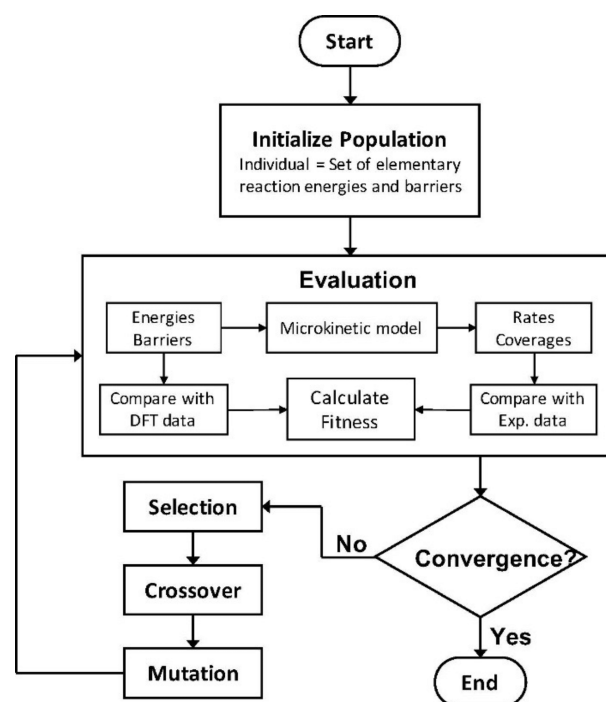

Figure 1. Overview of Genetic algorithm with Microkinetic Modeling.

coverage averaged over temperature and element (C,O) is denoted $\overline{C}$.

3. Agreement with DFT energies. While it is within the scope of the algorithm to alter the energies from DFT, it is important to control this process so that the results remain reasonable. Particularly, only a subset of all energies will affect the coverages, corresponding to rate-controlling steps for the overall rate. Thus, energies should only be altered if it leads to better experimental agreement fitness. To be more tolerant to small changes and more penalizing to large changes, the penalty is proportional to the square of the energy deviation averaged over all species, $\overline{E^2}$.

4. Adsorbate−adsorbate interaction. If a parameter is greater than a threshold, it is included and contributes with a constant penalty; if a parameter is smaller than a threshold, it is not included. The threshold was set to 0, under the approximation that only repulsive interactions will be of significance. The proportion of used AAI parameters, i.e., the number of used parameters divided by the number of possible AAI parameters, is denoted μ.

The fitness function is calculated as

$$f = c_S \overline{S} + \overline{C} + c_E \overline{E^2} + c_m \mu$$

where $c_S = 10, c_E = 1, c_m = 0.05$ are empirically determined coefficients, in order to prioritize the components in the order spectra, total coverage, DFT agreement, and AAI, while still having a noticeable impact from each term.

We used an initial population of 1000 individuals and subsequent populations of 200 individuals. The 100 fittest individuals were selected as parents, plus 20 more individuals at random (Selection). The fittest two individuals survive without changes to the next generation, and "children" are generated from two randomly selected parents from the pool above, by inheriting each gene from either parent at random (Crossover)

to make up the rest of the population. 10% of the "children" were mutated (Mutation); for each of these, a number of mutations between 1 and 13−17% of the total number of genes (4/32, 40/270, 50/292) was calculated at random; each mutation was carried out by first determining with equal probability an increase or decrease of the value and then selecting a uniformly random value between the current gene and the upper or the lower boundary. Convergence is defined as 250 generations without fitness improvement or reaching a maximum of 2000 generations. To improve optimization, we perform 50 runs with the same parameters, and then 5 more, where the fittest individuals among the 50 runs are included in the initial population. The developed Python code is available on GitHub.[40]

RESULTS AND DISCUSSION

Energies, barriers, and vibrations were calculated with DFT, and the raw data is available in the SI. Running the microkinetic model with the DFT-calculated energies and barriers without lateral interaction resulted in a coverage of >99% of a ML CO at all temperatures, in accordance with previous DFT results.[5,6] As the experimental CO coverages were <15% of a ML for all temperatures and the coverage of pure CO on Rh(111) is known to saturate at 75% of a ML,[35] it was clear that the adsorption energy of CO needed to be changed to match the experiment.

We calculated the C 1s binding energies of carbon-containing adsorbates, which are displayed in Table 1 in addition to

Table 1. C 1s Binding Energies (BEs) for Reaction Intermediates

	BE (eV)	Source	Used BE (eV)
CH2OH	284.95	This work	284.95
CH2O	284.61	This work	284.61
CH2	283.65	This work	283.80
	283.7	Solymosi[41]	
	283.9	Klivenyi[42]	
CH3O	285.98	This work	285.98
	285.7	Orozco (on Cu(111))[a43]	
CH3	284.05	This work (fcc)	284.35
	284.2	Solymosi[41]	
	284.5	Klivenyi[42]	
CHOH	284.83	This work	284.83
CHO	284.93	This work	284.93
CH	283.51	This work	283.70
	283.7	Vesseli[44]	
COH	285.21	This work	285.21
CO	286.00	Smedh[35]	286.00
C	283.64	This work	283.30
	283.3	Vesseli[44]	

[a]Experimental XPS binding energy for CH$_3$O on Rh is not available, so we approximate it with the reported binding energy on Cu(111).[43] Since the CH$_3$O species binds through the O atom rather than the C atom, the binding energy in a C 1s spectrum is not largely affected by the different metal substrates.

reported experimental data. The raw data is available in the SI. As described in the Method section, calculated values are calibrated so that the CO binding energy is equal to the experimental value of 286.0 eV. To simulate spectra from calculated coverages, we choose the experimental value (or averages if there are several), with the exception of CH$_3$O for which we only have the data on Cu(111), otherwise the DFT

value. When we allow XPS binding energies to be altered below, we allow a maximum change of 0.3 eV based on the spread of the data in the table.

GA with Altered Energies and Barriers. As a first illustration of the GA approach, we apply the GA to the MKM without including the adsorbate−adsorbate interaction (AAI) in the model, i.e., assuming that it is only a question of DFT uncertainties. This is intentional to demonstrate how the GA can be used to find deficiencies in the assumed MKM model. In Figures 2a and 2c, we show spectra and total C and O coverages, respectively, where the energies of gases, adsorbates and transition states are allowed to be altered by up to 0.3 eV, which is a reasonable margin with respect to typical DFT errors.[1,45] It is immediately clear that, even allowing these alterations, the XPS spectrum cannot be reproduced, as specifically seen in the coverage of CH$_x$ species (peak around 284 eV) at higher temperatures. The presence of a notable amount of CH is the only difference compared with applying the MKM with purely DFT energies (which leads to a surface poisoned by CO). We do not display the calculated hydrogen coverage, which lacks experimental data to be compared with the hydrogen coverage behaves like a Langmuir isotherm, which is expected in the model, as there is no competition for surface sites with other species and AAI is not included in the present case.

In Figures 2b and 2d we show that with larger energy margins (1.0, 0.5, and 0.3 eV for adsorbates, transition states, and gases, respectively), it is possible to approach an experimental fit within this MKM even in the absence of AAI. The CH$_x$ coverage at higher temperatures has now been pushed down (note the differences in scale between Figures 2a and 2b) at higher temperatures, but the agreement with experiment is not convincing. The total O coverage is worse than before, but as stated in the Method section, the O coverage is the least accurate of the experimental data. However, in terms of total C coverage, we find a significant improvement in the comparison with experiment. These larger energy margins are used for Figures 3 and 4, where we discuss the significant changes of the computed adsorption energies and barriers.

Figure 3 shows the changes introduced by the GA to the DFT computed adsorption energies, gas energies, and activation energies. The subscript 0 denotes coverage-independent energies which is trivial in the absence of AAI. Adsorbed CO is weakened by almost 0.8 eV, and consequently, the barriers to form COH and CHO are lowered; this prevents the CO poisoning with DFT values above and allows the reaction to move on. Note that the variable limited by ±0.5 eV is the transition state energy relative to gas phase, and that the shown activation energies in Figure 3b are relative to the adsorbate precursors. The strengthened adsorption of CH$_2$ and CH$_3$ and increase of the barriers to CH$_3$ and CH$_4$ increases the coverage of the former adsorbates (Figure 2d). It is not clear why H$_2$O adsorption is weakened (with a similar formation barrier).

In Figure 4, we compare energy landscapes with DFT energies and GA-generated energies for the reaction path with the highest rate obtained with the latter energies. This path produces methane and water.

We conclude that the GA manages to find modified adsorption energies and barriers that result in a clearly improved agreement with the experimental temperature-dependent coverages, but this requires an unphysically large change in the CO adsorption energy, leading to a much more weakly bound CO. Thus, the GA indicates that the effective CO adsorption energy should be weakened, which, in a more physical approach, can be
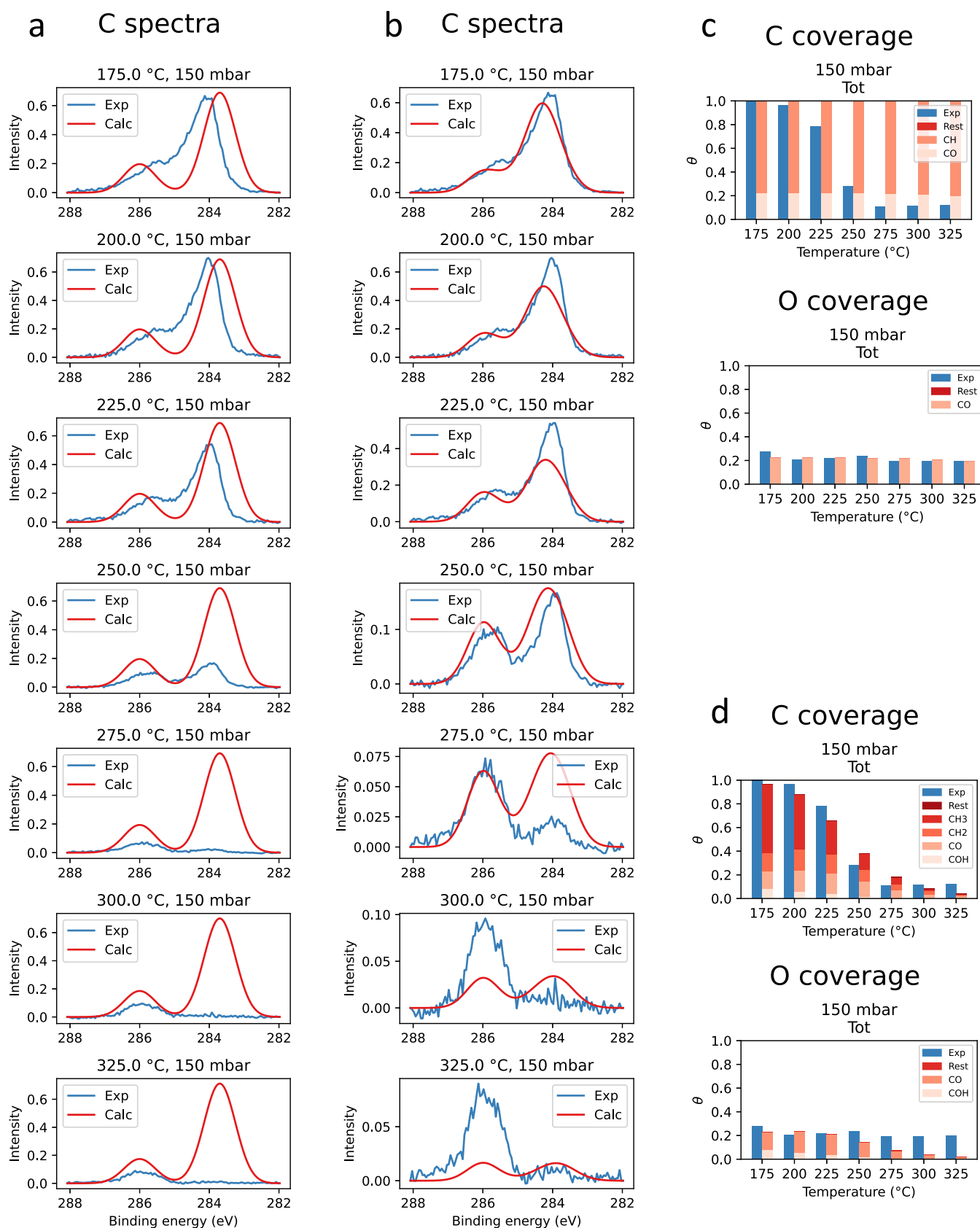
Figure 2. C 1s spectra (a, b; note the different *y* axis scales) and coverages (c,d) without AAI. Experimental data shown in blue and calculated in red. Specific (calculated) species are indicated by different shades of red. Changes in energies are limited to ±0.3 eV for all species in (a, c) and ±1.0, ± 0.5, ± 0.3 eV for adsorbates, transition states, and gases (b, d), respectively.
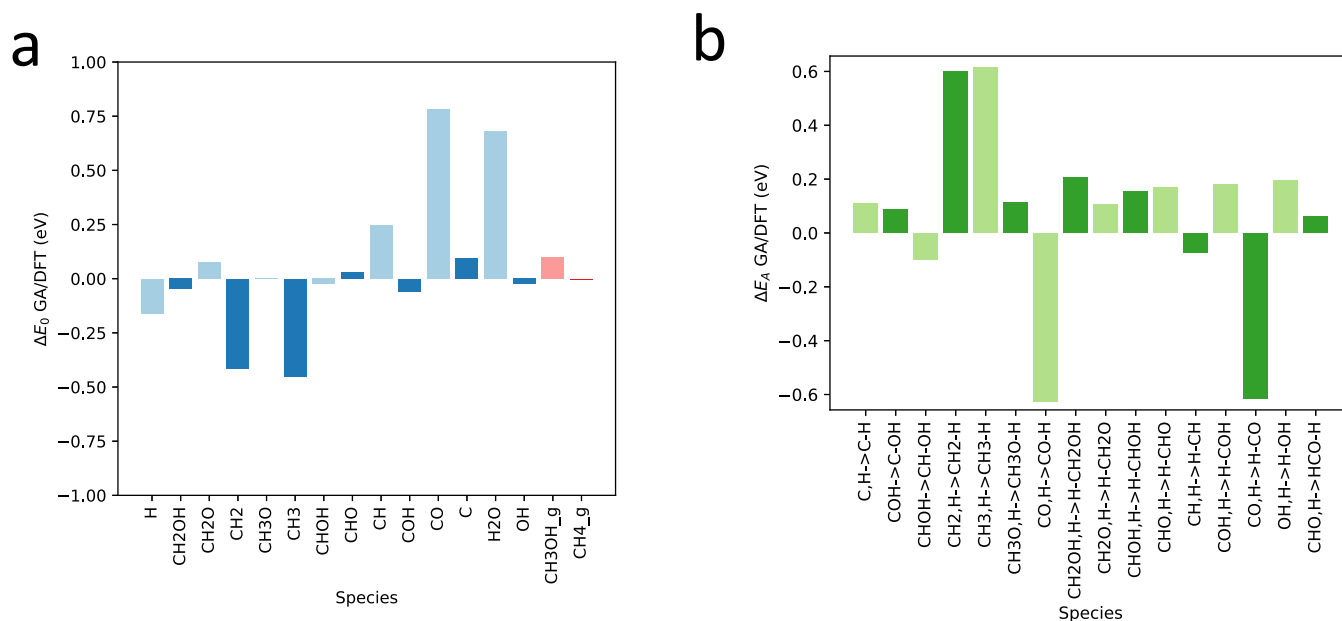
Figure 3. Difference between GA and DFT energy without AAI for (a) adsorbates (blue) and gas species (red, but barely visible), (b) activation energies (green).
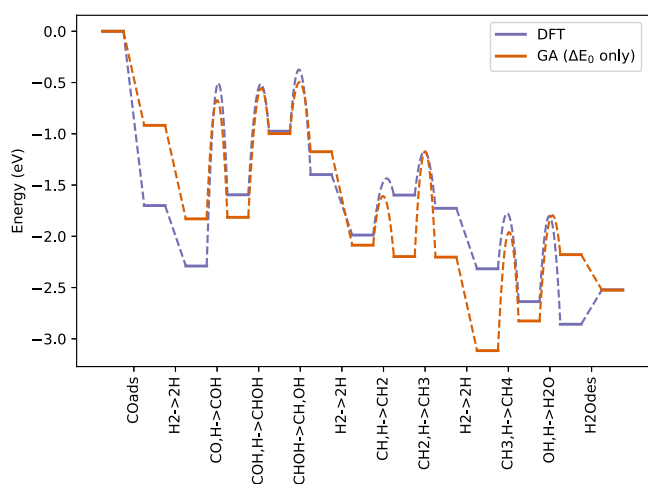
Figure 4. Energy landscape for the reaction with the highest rate. DFT energies are shown in blue and GA-generated energies in red. ΔE_0 denotes the coverage-independent part of the energy change, which in the absence of AAI is the entire change.

achieved by including the well-known adsorbate−adsorbate interaction (AAI) in the MKM.

Including AAI in the GA. Knowing that a larger energy change in CO adsorption energy is necessary, and similar to previous studies on the system[5,6] we extend the MKM to include adsorbate−adsorbate interaction in the GA. The linear parameters $m_{S,A}$ were allowed to vary in the interval $[0,1]$ and the energies by at most 0.3 eV. The optimized solution is shown in Figures 5-7 and in Table 2.

In Figure 5, we see that the inclusion of AAI has improved the fit to experiment significantly, compared to both energy margins in Figure 2. At high temperatures, the spectra agree very well, and at low temperatures, the peak at 284 eV matches experiment reasonably but with broader width of the calculated peak. However, the transitional regime at 250 and 275 °C is not captured to the same extent. The total C coverages agree well, with qualitatively the same adsorbates as with high energy

margins in Figure 2d. The model indicates notable coverages of COH, CH_2 and CH_3 at low temperatures. The O coverage at high temperatures is improved relative to the same settings, but still deviates from experiment at high temperatures.

In Figure 6, we see that the GA still alters the adsorbate, gas, and transition state energies significantly while still being within the assumed 0.3 eV range of DFT errors. In particular, CO and C adsorption are weakened while CH_2 and CH_3 adsorption are strengthened. The barriers to form CH_3, CH_4 and HCOH are increased, mainly following strengthening of precursor adsorption (including H), which can explain the increase in coverage of CH_2, CH_3 and COH. In addition to the coverage-independent adsorption energy, the AAI has a contribution. AAI parameters corresponding to self-interaction and TS cross interaction with notable adsorbates are shown in Table 2.

The interaction energy for CO comes from self-interaction ($0.89 * \theta_{CO}$, < 0.1 eV at all temperatures) and cross-interaction with the present coadsorbates CH_2, CH_3, COH, and H. As all of these have zero self-interaction parameter, and the cross-interaction is the average of the self-interaction parameters, the cross-interaction contributes with $0.44 * (\theta_{CH2} + \theta_{CH3} + \theta_{COH} + \theta_H)$, which is 0.88 eV at 175 °C. Similarly, the adsorption of C and CH are weakened by 0.77 and 0.71 eV, respectively. As the algorithm favors increased adsorption of CH_2, CH_3, and COH, it is reasonable that as little AAI is introduced for them as possible. Thus, they do not have a self-interaction slope, which means that they do not experience any self-interaction or interaction with each other, but only cross-interaction with CO ($0.44 * \theta_{CO}$). The fact that the GA does not introduce self-interaction for CH_2, CH_3, and COH (or H) should not be interpreted as an indication that it does not exist, but rather that the introduction of such interactions does not improve the fitness, i.e., the experimental fit or decrease the DFT deviation. Lastly, the transition states in the table have cross-interaction with adsorbates in a straightforward way, e.g., $0.8 * \theta_{COH}$, for $CH_2−H$. $CH_3−H$ is destabilized by 0.56 eV at 175 °C because of its interactions.
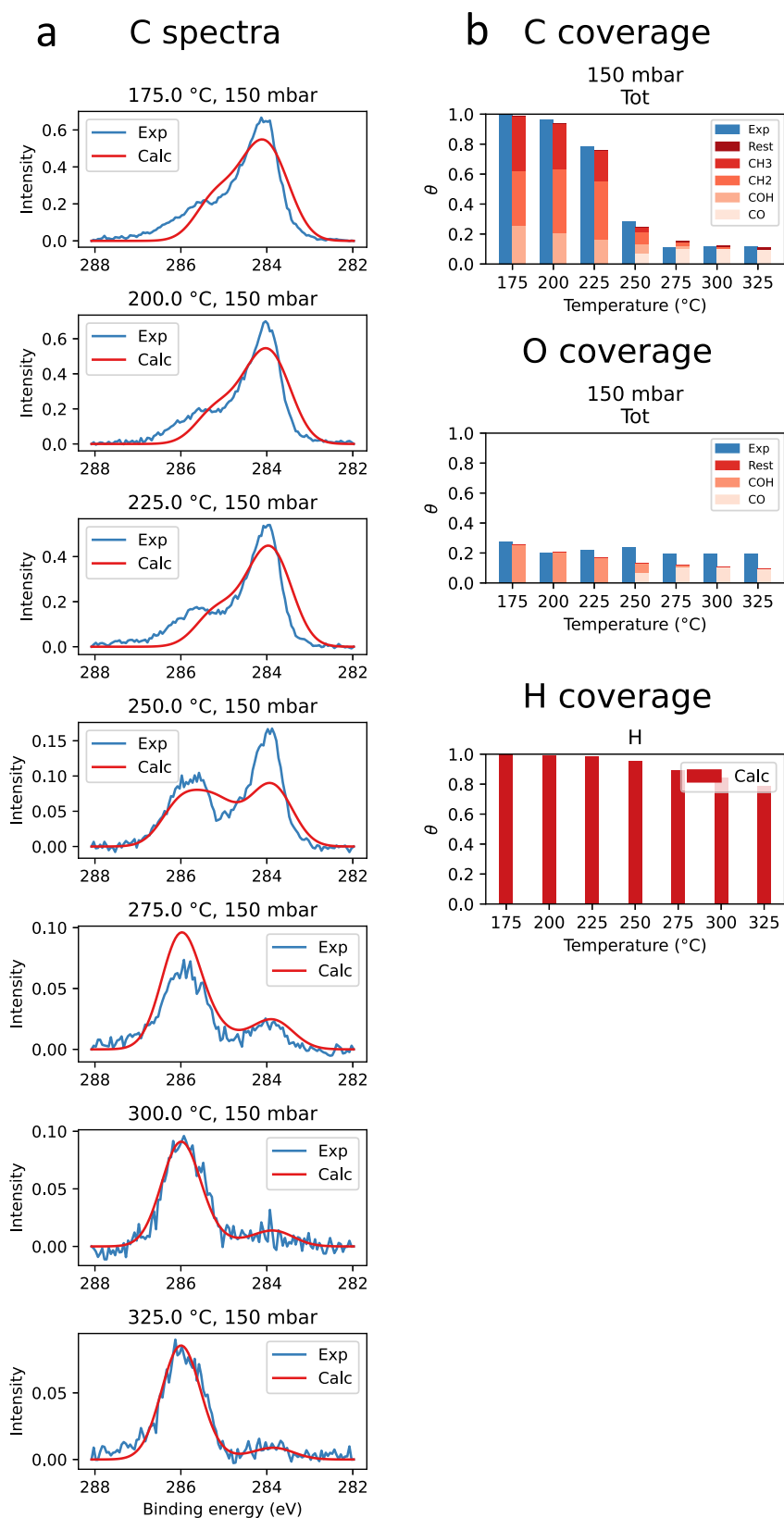
Figure 5. C 1s spectra and coverages with AAI and GA restricted to 0.3 eV adsorption/gas/transition state energy variations. Experimental data is shown in blue and calculated in red. Specific (calculated) species are indicated by different shades of red (b).

Figure 7 shows the energy landscapes for the reaction with highest rates after application of GA including AAI at 175 and 325 °C, compared to the same reaction with the AAI component removed for each surface species, and compared to the original DFT. The point is to visualize the components; e.g., for CO adsorption, the non-AAI energy change $\Delta E_0 = 0.25$ eV comes from Figure 6a and $\Delta E_{AAI} = 0.88$ eV at 325 °C due to high coadsorbate coverage discussed above.
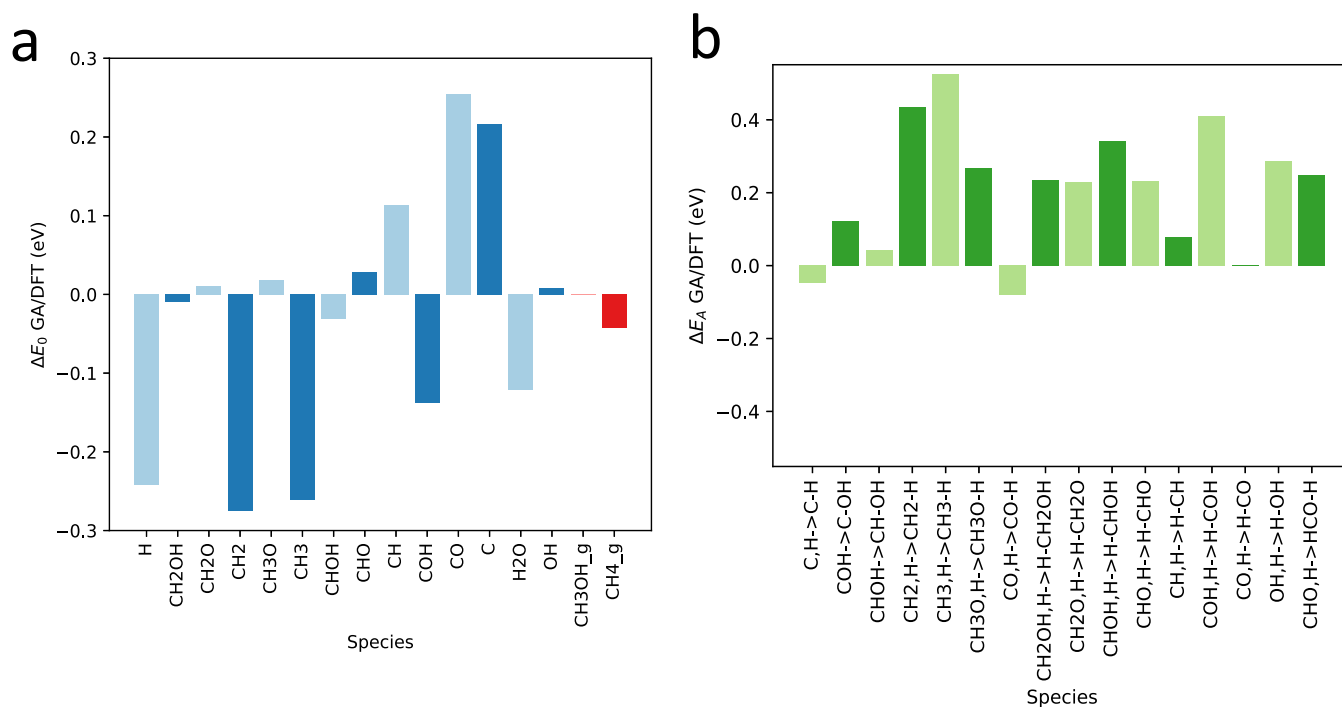
Figure 6. Difference between coverage-independent (non-AAI) part of GA and DFT energy with AAI included in the algorithm for (a) adsorbates (blue) and gas species (red), (b) activation energies (green).
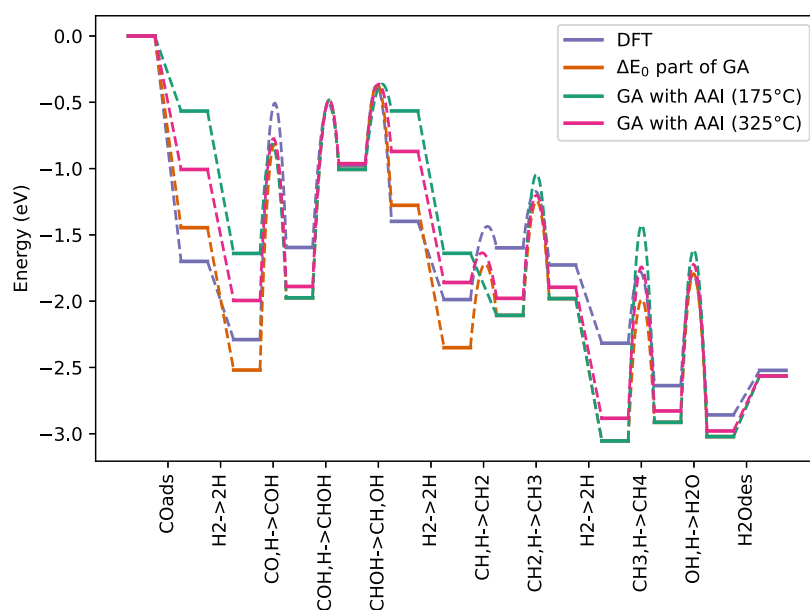
Figure 7. Energy landscape for the reaction with highest rate with AAI included. Pure DFT data is shown in blue. The coverage-independent (non-AAI) part of the GA-generated energy change is shown in red. The full GA-generated data including AAI is shown in green (175 °C) and magenta (325 °C).

Table 2. GA Self-Interaction Slopes for Notable Adsorbates and Slopes with Transition States[a]

	CO	COH	CH$_2$	CH$_3$	C	CH	H
self-inter.	0.89				0.78	0.72	
CH$_2$–H		0.8					
CH$_3$–H	0.39	0.95	0.06	0.39			0.15
H–OH				0.25			0.09

[a]Empty cells indicate lack of interaction.

From these results, we can conclude that it is possible to explain the main disagreements between pure DFT and experiment with reasonable DFT uncertainties plus AAI. We do not suggest that our AAI model is "correct", but rather simple enough to work within our GA variable framework and indicate whether AAI *could* be enough.

Allowing Altered BE Peaks and Broadening. The spectra fit in Figure 5a could be improved, so we investigate if it can be explained by small changes in the XPS parameters. Thus, as a last addition to the GA, we allow the XPS BE peaks
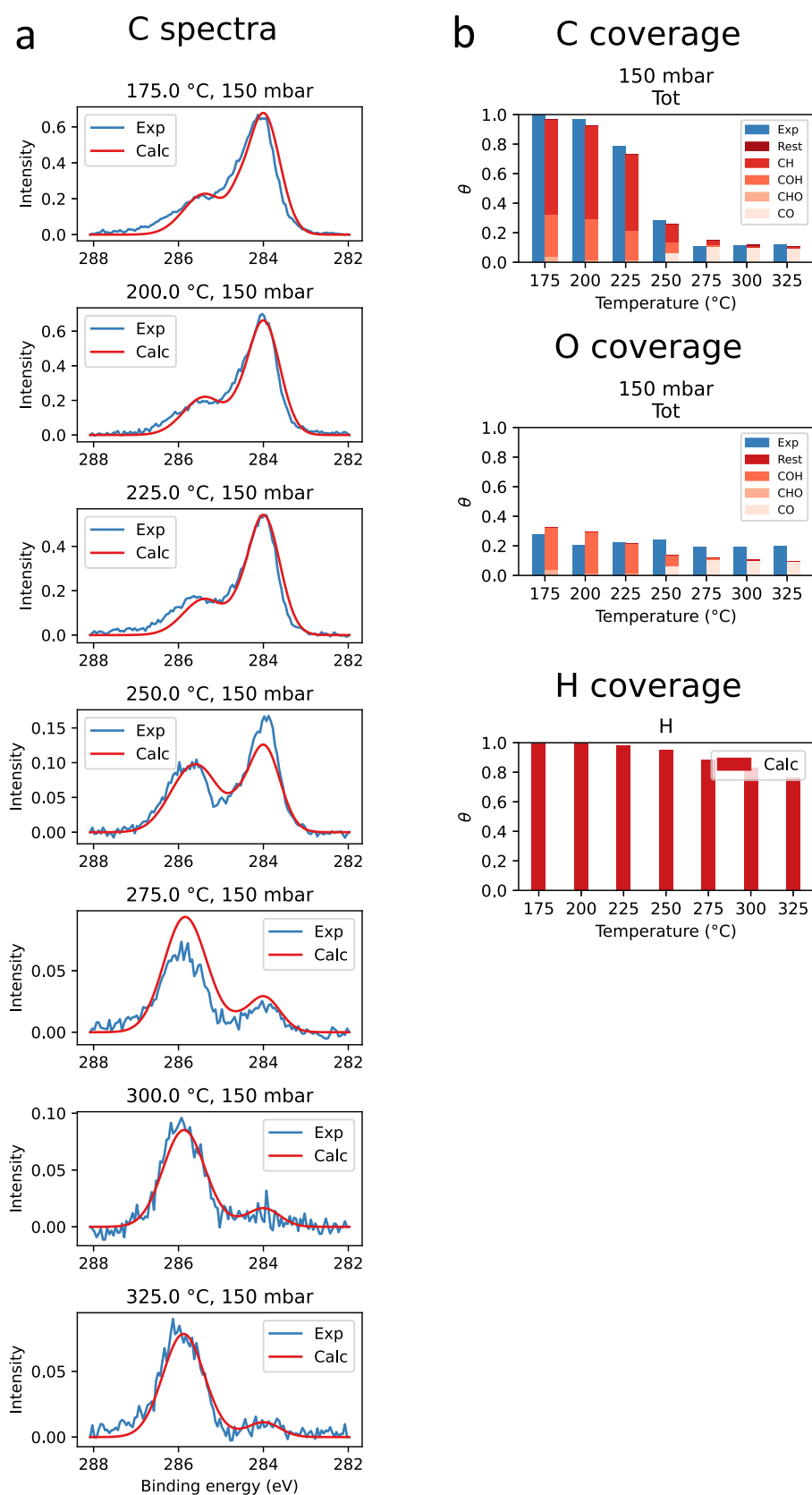
Figure 8. C 1s spectra and coverages with AAI and variable XPS peaks and broadenings. Experimental data is shown in blue and calculated in red.

and broadening (σ, the standard deviation of the normal distribution) to vary. We allow a range of 0.3 eV around the computed or chosen value in Table 1, which notably allows the variation to cover both computed and experimental values for

the binding energies shown in the table. Noting that the calculated peak at 284 eV at low temperatures in Figure 5 is too broad, we set the range of σ to $[0.2, 0.5]$ eV, i.e., mostly lower than the value based on the 286 eV peak at high temperatures

(0.45 eV). The lower end of the range is determined by the limit of the photon bandwidth and analyzer resolution in the experiment, while the upper end is based on the observed width of the peaks in the raw data. We do not add any penalty for changes; the point of a penalty is to single out the most important contributions, and in this case, these are the adsorbates with notable coverage.

Figure 8 shows the spectra and total coverages with AAI and variable XPS peaks and broadenings. The spectra are now in good agreement, though not perfect at the transitional temperatures of 250 and 275 °C. However, while the total C coverages agree well, the adsorbate distribution is different from before, compared to CH_2 and CH_3 contributions in Figures 2d and 5b. At low temperatures, it is now CH that dominates. As can be seen from the GA-generated XPS BEs and broadenings in Table 3, the CH peak is moved by the maximum amount to

Table 3. GA-Generated XPS Binding Energies, the Change from the Previously Used BEs (Experimental Value on Rh(111) if Possible, otherwise DFT), and Broadening Parameter σ

	GA BE (eV)	ΔBE (rel. to used BE)	σ (eV)
CH_2OH	284.95	0.00	0.27
CH_2O	284.66	+0.05	0.21
CH_2	284.00	+0.20	0.49
CH_3O	286.26	+0.28	0.26
CH_3	284.52	+0.17	0.24
CHOH	284.79	−0.04	0.35
CHO	284.63	−0.30	0.20
CH	284.00	+0.30	0.38
COH	285.38	+0.17	0.50
CO	285.89	−0.11	0.48
C	283.17	−0.13	0.37

higher energy, ending up at the 284 eV peak in the spectra. The CH_2 peak is also changed to 284 eV, so in isolation, it could have been responsible for the peak. However, high CH_2 coverage required strengthening of the CH_2 adsorption energy in Figures 3a and 6a; thus, as CH coverage replaces CH_2 coverage, there is no need for the CH_2 energy change, as seen in Figure 9a. If the BE parameter range is smaller, e.g., ±0.15 eV instead of ±0.3 eV, the CH peak cannot shift enough, leading to the previously observed behavior of CH_3, CH_2, and COH domination at lower temperatures. We show this effect in the SI.

The other changes in XPS BE in Table 3 relating to adsorbates with notable coverage (COH, CO) and adsorbates with notable coverage in previous runs (CH_2, CH_3) are smaller. The broadening of the CH peak is less than the previously fixed 0.45 eV, as expected, but the COH and CO broadenings remain high.

In Figure 9a, no change is applied by the GA to CH_2 and CH_3 adsorption, as these adsorbates in this case do not contribute to the coverage. Instead, CHO adsorption is strengthened, which only results in a small impact regarding coverages. Otherwise, the COH and H strengthening, and the CO weakening are in line with previous results in Figure 6a. Regarding activation energies in Figure 9b, it mostly follows from the adsorption energies that barriers from CHO are increased the most. The barriers are increased more, generally speaking, than in Figure 6b.

The important AAI parameters can be seen in Table 4. Similar to in Table 2, the CO and C cross-interaction with the significant adsorbates (in this case CH, COH, and H) with the average parameter of self-interactions, i.e., 0.41, contributes the most to the energy correction, which sums up to 0.82 and 0.76 eV at 175 °C for CO and C, respectively. Compared to the case without altered peak parameters, more transition states have significant interaction.
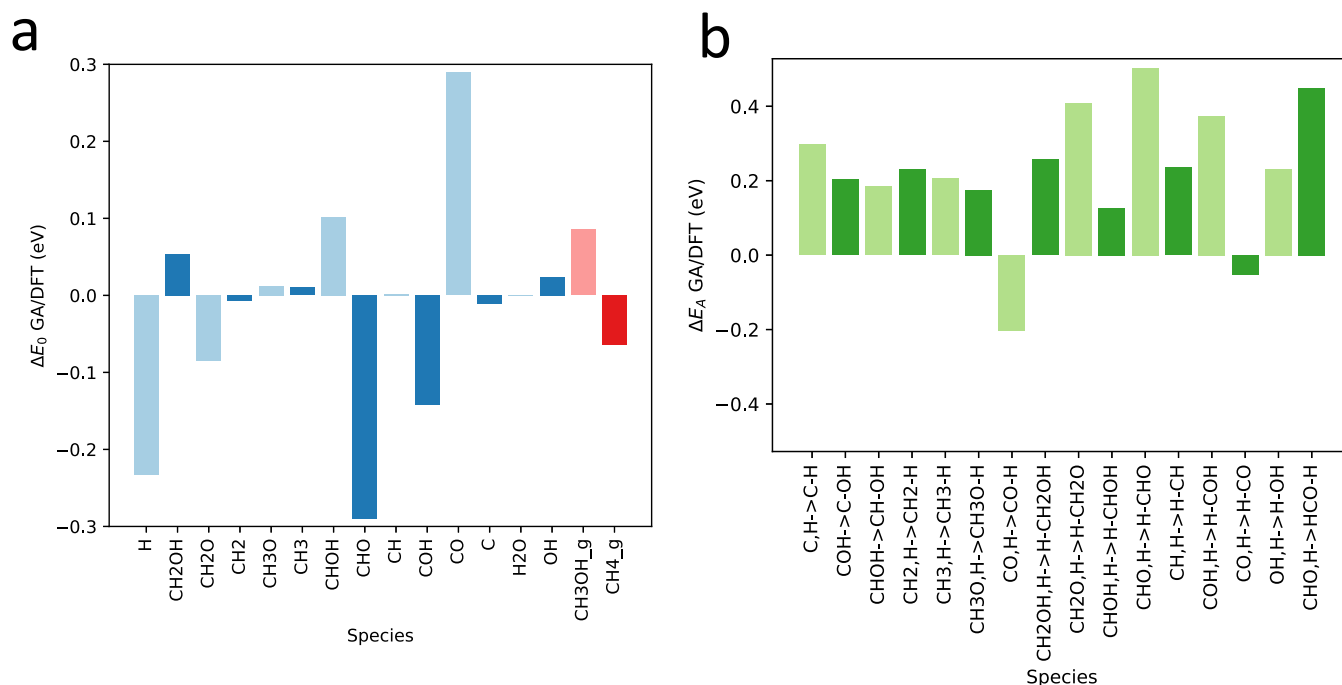
Figure 9. Difference between coverage-independent (non-AAI) part of GA and DFT energy for (a) adsorbates (blue) and gas species (red), (b) activation energies (green), with AAI and variable XPS peaks and broadenings in the algorithm.

Table 4. GA Self-Interaction Slopes for Notable Adsorbates and Slopes with Transition States, with Variable XPS Peaks and Broadenings in the Algorithm[a]

	CO	COH	CH$_2$	C	H
self-inter.	0.84			0.77	
C−OH					0.91
CH$_2$−H	0.68				
CH$_3$−H	0.92	0.98			
CO-H		0.63			0.69
H−COH					0.97
H−CO			0.93		

[a]Empty cells indicate lack of interaction.

In Figure 10, we see that the reaction path with highest rate has changed from Figure 7, going through CHO rather than COH. This is interesting, as the coverage of COH is higher than CHO, but it is possible that the reaction paths through COH are slower. The AAI impact is moderate in comparison with Figure 7, with the exception of CO adsorption.

Allowing altered XPS BEs and broadenings improved the spectrum fit, with changed coverage distribution and dominant reaction path. Either the CH$_2$ adsorption energy or the CH XPS binding energy needs to be altered to fit to experiment, in addition to, e.g., CO adsorption weakening. While caution needs to be exercised in the process, the introduction of variation in the XPS peak parameters can give direction for spectrum interpretation in cases where the accuracies of both computed and experimental reference spectra are uncertain.

A natural extension is to add reaction steps leading to C$_{2+}$ species, as there are, e.g., ethanol intermediates that could have similar C XPS binding energies and thus contribute to the observed high coverages of hydrocarbon species, i.e. some CH$_x$ species being C$_y$H$_x$ allowing multiple carbons associated with a Rh atom. Another possible next step is to study the adsorbates and barriers, that needed altered energies, on edges or defects. Inclusion of such sites—even though the experiment was performed on single-crystal Rh(111) − may be justified as single-crystals can have a defect density of 1 per 20th unit cell. The induced defect density may be particularly high under operating conditions with strongly interacting molecules, such as CO. Although not the case here at 150 mbar pressure, it has been observed previously[20] that at a higher pressure of 2 bar undercoordinated adatoms may move from the lattice onto the surface. Furthermore, the presence of step sites and point defects has been shown to destabilize CO on Rh,[46] in accordance with the prediction of the GA.

Of course, species needing AAI should be considered with a more realistic model of AAI, such as in ref.,[5,47,48] and higher orders of electronic structure calculations can be considered for the species with large energy changes. Note that, AAI involving hydrogen is included in the MKM even though hydrogen is treated as a reservoir and does not compete for sites.

However, we limit ourselves in the present work to the proof of concept with the coupled genetic algorithm and MKM modeling to compare with experimental high-pressure XPS data. The method can be expanded to a wide range of models of heterogeneous catalysis and provide a new method of construction and validation.

CONCLUSIONS

To improve microkinetic modeling based on DFT calculations, which is an important tool to better understand reaction mechanisms in heterogeneous catalysis, we have developed and applied a genetic algorithm (GA) to modify the parameters of the microkinetic (MKM) model to target a reference experiment. Given a microkinetic model of CO hydrogenation to methanol, methane and water on Rh(111), we investigated what energies and barriers would need to be changed in the MKM to agree with experimental coverage data determined under reaction conditions using high-pressure XPS. We found that CO adsorption must be substantially weaker relative to the computed DFT energy. However, introducing a simple, linear adsorbate−adsorbate interaction allows the changes of low-
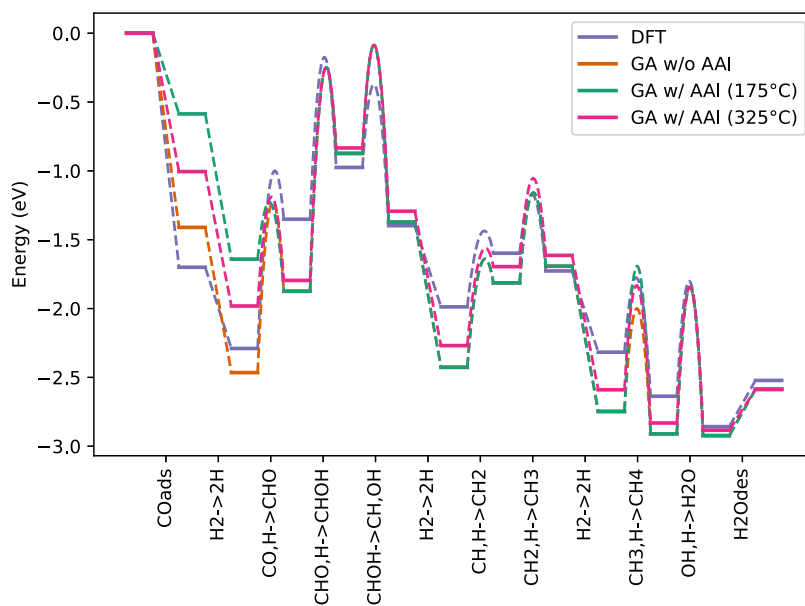
Figure 10. Energy landscape for the reaction with highest rate with AAI and variable XPS peaks and broadenings included in the algorithm. Pure DFT data is shown in blue. The coverage-independent (non-AAI) part of the GA-generated energy change is shown in red. The full GA-generated data including AAI is shown in green (175 °C) and magenta (325 °C).

coverage adsorption energy to remain <0.3 eV and improves the experimental fit. Furthermore, letting the XPS binding energies and broadenings vary, improves the spectrum fit even further, with changed coverage distribution and preferred pathway. This opens up a question on what is more reliable: adsorption energies or XPS binding energies. We conclude that the model indicates the need for more complexity, such as, e.g., expansion of the model with C2 species, introducing edges or defects, going to higher orders of electronic structure calculations.

The GA in combination with the temperature-dependent coverages in terms of XPS peaks has thus highlighted problems with the initial DFT MKM model. We propose that the combination of GA and MKM and now available detailed coverage data can be used to iteratively increase the accuracy of a given MKM, together with interpretation and hypothesis testing. The GA approach can be used as a complement and test of DFT in heterogeneous catalysis in general when reliable coverage data, such as the present, becomes available.

ASSOCIATED CONTENT

Data Availability Statement
The data that support the findings of this study are available in the Supporting Information.

Ⓢ Supporting Information
The Supporting Information is available free of charge at https://pubs.acs.org/doi/10.1021/acs.jpcc.4c02020.

> DFT energies and vibrations and results corresponding to Figures 8 and 9, but with ±0.15 eV bounds on XPS energies (PDF)

> Python code for MKM with GA, data for DFT energy, vibration and XPS calculations, as well as genetic algorithm calculations. The program for MKM with GA is also available on GitHub.[40] (ZIP)

AUTHOR INFORMATION

Corresponding Author
Lars G. M. Pettersson − *Department of Physics, Stockholm University, 109 61 Stockholm, Sweden*; Email: lgm@fysik.su.se

Authors
Mikael Valter-Lithander − *Department of Physics, Stockholm University, 109 61 Stockholm, Sweden*; ⓞ orcid.org/0000-0002-7718-3525

Minttu Kauppinen − *Department of Physics and Competence Centre for Catalysis, Chalmers University of Technology, 41296 Göteborg, Sweden*; ⓞ orcid.org/0000-0001-8721-3719

David Degerman − *Department of Physics, Stockholm University, 109 61 Stockholm, Sweden*; ⓞ orcid.org/0000-0001-6085-2916

Gabriel L. S. Rodrigues − *Department of Physics, Stockholm University, 109 61 Stockholm, Sweden*

Henrik Grönbeck − *Department of Physics and Competence Centre for Catalysis, Chalmers University of Technology, 41296 Göteborg, Sweden*

Complete contact information is available at:
https://pubs.acs.org/10.1021/acs.jpcc.4c02020

Notes
The authors declare no competing financial interest.

REFERENCES
(1) Medford, A. J.; Lausche, A. C.; Abild-Pedersen, F.; Temel, B.; Schjødt, N. C.; Nørskov, J. K.; Studt, F. Activity and selectivity trends in synthesis gas conversion to higher alcohols. *Top. Catal.* **2014**, *57*, 135−142.

(2) Motagamwala, A. H.; Dumesic, J. A. Microkinetic modeling: A tool for rational catalyst design. *Chem. Rev.* **2021**, *121*, 1049−1076.

(3) Wittreich, G. R.; Alexopoulos, K.; Vlachos, D. G. Microkinetic modeling of surface catalysis. In *Handbook of materials modeling*, Andreoni, W., Yip, S., Eds. Springer Nature: Switzerland AG, 2020; pp 1377−1402.

(4) Wellendorff, J.; Lundgaard, K. T.; Møgelhøj, A.; Petzold, V.; Landis, D. D.; Nørskov, J. K.; Bligaard, T.; Jacobsen, K. W. Density functionals for surface science: Exchange-correlation model development with bayesian error estimation. *Phys. Rev. B* **2012**, *85*, 235149.

(5) Yang, N.; Medford, A. J.; Liu, X.; Studt, F.; Bligaard, T.; Bent, S. F.; Nørskov, J. K. Intrinsic selectivity and structure sensitivity of rhodium catalysts for C_{2+} oxygenate production. *J. Am. Chem. Soc.* **2016**, *138*, 3705−3714.

(6) Schumann, J.; Medford, A. J.; Yoo, J. S.; Zhao, Z.-J.; Bothra, P.; Cao, A.; Studt, F.; Abild-Pedersen, F.; Nørskov, J. K. Selectivity of synthesis gas conversion to C_{2+} oxygenates on fcc(111) transition-metal surfaces. *ACS Catal.* **2018**, *8*, 3447−3453.

(7) Gu, T.; Wang, B.; Chen, S.; Yang, B. Automated generation and analysis of the complex catalytic reaction network of ethanol synthesis from syngas on Rh(111). *ACS Catal.* **2020**, *10*, 6346−6355.

(8) Wind, T. L.; Falsig, H.; Sehested, J.; Moses, P. G.; Nguyen, T. T. M. Comparison of mechanistic understanding and experiments for CO methanation over nickel. *J. Catal.* **2016**, *342*, 105−116.

(9) Bhandari, S.; Rangarajan, S.; Mavrikakis, M. Combining computational modeling with reaction kinetics experiments for elucidating the in situ nature of the active site in catalysis. *Acc. Chem. Res.* **2020**, *53*, 1893−1904.

(10) Araujo, R. B.; Rodrigues, G. L. S.; Campos dos Santos, E.; Pettersson, L. G. M. Adsorption energies on transition metal surfaces: Towards an accurate and balanced description. *Nature Commun.* **2022**, *13*, 6853.

(11) Sauer, J. Ab initio calculations for molecule-surface interactions with chemical accuracy. *Acc. Chem. Res.* **2019**, *52*, 3502−3510.

(12) Alessio, M.; Usvyat, D.; Sauer, J. Chemically accurate adsorption energies: CO and H_2O on the MgO(001) surface. *J. Chem. Theory Comput.* **2019**, *15*, 1329−1344.

(13) Sheldon, C.; Paier, J.; Usvyat, D.; Sauer, J. Hybrid RPA:DFT approach for adsorption on transition metal surfaces: Methane and ethane on platinum (111). *J. Chem. Theory Comput.* **2024**, *20*, 2219−2227.

(14) Ulissi, Z. W.; Medford, A. J.; Bligaard, T.; Nørskov, J. K. To address surface reaction network complexity using scaling relations machine learning and DFT calculations. *Nature Commun.* **2017**, *8*, 14621.

(15) Rangarajan, S.; Maravelias, C. T.; Mavrikakis, M. Sequential-optimization-based framework for robust modeling and design of heterogeneous catalytic systems. *J. Phys. Chem. C* **2017**, *121*, 25847−25863.

(16) Bhandari, S.; Rangarajan, S.; Maravelias, C. T.; Dumesic, J. A.; Mavrikakis, M. Reaction mechanism of vapor-phase formic acid decomposition over platinum catalysts: DFT, reaction kinetics experiments, and microkinetic modeling. *ACS Catal.* **2020**, *10*, 4112−4126.

(17) Amann, P.; Degerman, D.; Lee, M.-T.; Alexander, J. D.; Shipilin, M.; Wang, H.-Y.; Cavalca, F.; Weston, M.; Gladh, J.; Blom, M.; et al. A high-pressure x-ray photoelectron spectroscopy instrument for studies of industrially relevant catalytic reactions at pressures of several bars. *Rev. Sci. Instrum.* **2019**, *90*, 103102.

(18) Degerman, D.; Lömker, P.; Goodwin, C. M.; Shipilin, M.; García-Martínez, F.; Schlueter, C.; Nilsson, A.; Amann, P. State of the surface during co hydrogenation over Ni(111) and Ni(211) probed by operando x-ray photoelectron spectroscopy. *J. Phys. Chem. C* **2023**, *127*, 4021−4032.

(19) Shipilin, M.; Degerman, D.; Lömker, P.; Goodwin, C. M.; Rodrigues, G. L. S.; Wagstaffe, M.; Soldemo, M.; Gladh, J.; Wang, H.-Y.; Stierle, A.; et al. In situ surface-sensitive investigation of multiple carbon phases on Fe(110) in Fischer−Tropsch synthesis. *ACS Catal.* **2022**, *12*, 7609−7621.

(20) Degerman, D.; Goodwin, C. M.; Lömker, P.; García-Martínez, F.; Shipilin, M.; Gloskovskii, A.; Nilsson, A. Demonstrating pressure jumping as a tool to address the pressure gap in high pressure photoelectron spectroscopy of CO and CO$_2$ hydrogenation on Rh(211). *ChemPhysChem* **2024**, *25*, No. e202300523.

(21) Goodwin, C. M.; Lömker, P.; Degerman, D.; Davies, B.; Shipilin, M.; Garcia-Martinez, F.; Koroidov, S.; Mathiesen, J. K.; Rameshan, R.; Rodrigues, G. L. S.; et al. Operando probing of the surface chemistry during the Haber-Bosch process. *Nature* **2024**, *625*, 282−286.

(22) Amann, P.; Klötzer, B.; Degerman, D.; Köpfle, N.; Götsch, T.; Lömker, P.; Rameshan, C.; Ploner, K.; Bikaljevic, D.; Wang, H.-Y.; et al. The state of zinc in methanol synthesis over a Zn/ZnO/Cu(211) model catalyst. *Science* **2022**, *376*, 603−608.

(23) Degerman, D.; Shipilin, M.; Lömker, P.; Goodwin, C. M.; Gericke, S. M.; Hejral, U.; Gladh, J.; Wang, H.-Y.; Schlueter, C.; Nilsson, A.; et al. Operando observation of oxygenated intermediates during CO hydrogenation on Rh single crystals. *J. Am. Chem. Soc.* **2022**, *144*, 7038−7042.

(24) Chen, Z.; Wang, H.; Liu, Z.; Xu, X. Dynamic and intermediate-specific local coverage controls the syngas conversion on Rh(111) surfaces: An operando theoretical analysis. *ACS Catal.* **2021**, *11*, 3830−3841.

(25) Deimel, M.; Prats, H.; Seibt, M.; Reuter, K.; Andersen, M. Selectivity trends and role of adsorbate-adsorbate interactions in CO hydrogenation on rhodium catalysts. *ACS Catal.* **2022**, *12*, 7907−7917.

(26) Kresse, G.; Furthmüller, J. Efficient iterative schemes for ab initio total-energy calculations using a plane-wave basis set. *Phys. Rev. B* **1996**, *54*, 11169−11186.

(27) Kresse, G.; Furthmüller, J. Efficiency of ab-initio total energy calculations for metals and semiconductors using a plane-wave basis set. *Comput. Mater. Sci.* **1996**, *6*, 15−50.

(28) Kresse, G.; Hafner, J. Ab initio molecular dynamics for liquid metals. *Phys. Rev. B* **1993**, *47*, 558−561.

(29) Kresse, G.; Hafner, J. Ab initio molecular-dynamics simulation of the liquid-metal-amorphous-semiconductor transition in germanium. *Phys. Rev. B* **1994**, *49*, 14251−14269.

(30) Blöchl, P. E. Projector augmented-wave method. *Phys. Rev. B* **1994**, *50*, 17953.

(31) Jónsson, H.; Mills, G.; Jacobsen, K. W. Nudged elastic band method for finding minimum energy paths of transitions. In *Classical and quantum dynamics in condensed phase simulations*, Berne, B. J., Ciccotti, G., Coker, D. F., Eds. World Scientific: 1998; p 385.

(32) Henkelman, G.; Jónsson, H. A dimer method for finding saddle points on high dimensional potential surfaces using only first derivatives. *J. Chem. Phys.* **1999**, *111*, 7010−7022.

(33) Henkelman, G.; Uberuaga, B. P.; Jónsson, H. A climbing image nudged elastic band method for finding saddle points and minimum energy paths. *J. Chem. Phys.* **2000**, *113*, 9901−9904.

(34) Takahashi, O.; Pettersson, L. G. M. Functional dependence of core-excitation energies. *J. Chem. Phys.* **2004**, *121*, 10339−10345.

(35) Smedh, M.; Beutler, A.; Borg, M.; Nyholm, R.; Andersen, J. N. Determination of the coverage dependent isosteric heat of adsorption of CO on Rh(111) by high resolution core level photoemission. *Surf. Sci.* **2001**, *491*, 115−123.

(36) Shirley, D. A. High-resolution x-ray photoemission spectrum of the valence bands of gold. *Phys. Rev. B* **1972**, *5*, 4709−4714.

(37) Lausche, A. C.; Medford, A. J.; Suvra Khan, T.; Xu, Y.; Bligaard, T.; Abild-Pedersen, F.; Nørskov, J. K.; Studt, F. On the effect of coverage-dependent adsorbate-adsorbate interactions for CO methanation on transition metal surfaces. *J. Catal.* **2013**, *307*, 275−282.

(38) Hjorth Larsen, A.; Mortensen, J. J.; Blomqvist, J.; Castelli, I. E.; Christensen, R.; Dułak, M.; Friis, J.; Groves, M. N.; Hammer, B.; Hargus, C.; et al. The atomic simulation environment—a Python library for working with atoms. *J. Phys.: Condens. Matter* **2017**, *29*, 273002.

(39) Virtanen, P.; Gommers, R.; Oliphant, T. E.; Haberland, M.; Reddy, T.; Cournapeau, D.; Burovski, E.; Peterson, P.; Weckesser, W.; Bright, J.; et al. Scipy 1.0: Fundamental algorithms for scientific computing in Python. *Nat. Methods* **2020**, *17*, 261−272.

(40) Valter-Lithander, M.; Kauppinen, M. *Python code for MKM with GA*, 2024. https://github.com/Lillejanur/gamkm.

(41) Solymosi, F. Thermal stability and reactions of CH$_2$, CH$_3$ and C$_2$H$_5$ species on the metal surfaces. *Catal. Today* **1996**, *28*, 193−203.

(42) Klivényi, G.; Solymosi, F. Generation of CH$_2$ species: Thermal and photo-induced dissociation of CH$_2$I$_2$ on Rh(111) surface. *Surf. Sci.* **1995**, *342*, 168−184.

(43) Orozco, I.; Huang, E.; Mahapatra, M.; Kang, J.; Shi, R.; Nemšák, S.; Tong, X.; Senanayake, S. D.; Liu, P.; Rodríguez, J. A. Understanding methanol synthesis on inverse ZnO/CuO$_x$/Cu catalysts: Stability of CH$_3$O species and dynamic nature of the surface. *J. Phys. Chem. C* **2021**, *125*, 6673−6683.

(44) Vesselli, E.; Baraldi, A.; Comelli, G.; Lizzit, S.; Rosei, R. Ethanol decomposition: C-C cleavage selectivity on Rh(111). *ChemPhysChem* **2004**, *5*, 1133−1140.

(45) Wellendorff, J.; Lundgaard, K. T.; Jacobsen, K. W.; Bligaard, T. Mbeef: An accurate semi-local bayesian error estimation density functional. *J. Chem. Phys.* **2014**, *140*, 144107.

(46) Mavrikakis, M.; Bäumer, M.; Freund, H.-J.; Nørskov, J. K. Structure sensitivity of CO dissociation on Rh surfaces. *Catal. Lett.* **2002**, *81*, 153−156.

(47) Goswami, A.; Schneider, W. F. Mean field model parameterization to recover coverage-dependent kinetics. *J. Catal.* **2023**, *426*, 352−360.

(48) Bajpai, A.; Frey, K.; Schneider, W. F. Comparison of coverage-dependent binding energy models for mean-field microkinetic rate predictions. *Langmuir* **2020**, *36*, 465−474.